Graphene nanoribbon-TiO_2-quantum dots hybrid photoanode to boost the performance of photoelectrochemical for hydrogen generation

Rusoma Akilimali[a], Gurpreet Singh Selopal[a,b,*], Daniele Benetti[a], Mahyar Mohammadnezhad[a], Haiguang Zhao[c,**], Zhiming M. Wang[b], Barry Stansfield[a], Federico Rosei[a,b,*]

[a] Institut National de la Recherche Scientifique, Centre Énergie, Matériaux et Télécommunications, 1650 Boul. Lionel Boulet Varennes, Québec, J3X 1S2, Canada
[b] Institute of Fundamental and Frontier Sciences, University of Electronic Science and Technology of China, Chengdu, 610054, PR China
[c] The State Key Laboratory & College of Physics, Qingdao University, No. 308 Ningxia Road, Qingdao, 266071, PR China

A B S T R A C T

We report the effect of incorporation of graphene nanoribbons (GNR) into a TiO_2 mesoporous film sensitized with colloidal CdSe/CdS core/shell quantum dots (QDs) on the efficiency and long-term stability of a photoelectrochemical (PEC) cell for hydrogen (H_2) generation. The GNR-TiO_2 hybrid photoanodes were prepared by using simple, low-cost and large-area scalable doctor-blade method. The presence of GNR in the hybrid photoanode was confirmed by ultraviolet-visible absorption measurements, scanning electron microscopy and Raman spectroscopy. Our results demonstrate that an optimum loading of 0.02 wt% GNR increases the photocurrent density (at 0.8 V vs RHE) of the PEC device up to 5.51 mA/cm^2, which is 30% higher than that of the control device. This improvement in photocurrent density can be attributed to enhanced electron transport (reduced charge transport resistance) in GNR-TiO_2 hybrid anodes as confirmed by electrochemical impedance spectroscopy. In addition, PEC cells based on GNRs-TiO_2/QDs hybrid photoanode maintain ~65% of the initial photocurrent density after 7200 s of continuous one sun illumination, which is 15% higher than PEC cell based on a standard TiO_2/QDs photoanode. Our findings offer a simple, large area scalable and low-cost approach to fabricate photoanode for high-performance optoelectronic devices, such as improving the performance of PEC cells for hydrogen generation.

1. Introduction

Hydrogen (H_2) is a promising high-energy density clean fuel that can provide renewable and sustainable energy [1,2]. Presently H_2 is primarily used in applications such as petroleum refining [3,4], ammonia production [5,6] and to a lesser extent in metal refining in the mining industry [7,8]. Although the majority of energy used in transportable and storable energy sources still comes from fossil fuels, substantive efforts are made to produce H_2 from widely available feedstock like water and solar driven processes, which has the capacity to provide ample energy to meet human need and tackle environmental issues [9–13]. Renewable H_2 production can be driven by different technologies [14–16], among which Photoelectrochemical (PEC) solar-fuel conversion is a promising and clean approach to produce storable fuel from solar radiation [17,18]. A PEC device consists of a photoanode, an electrolyte and a counter electrode [see Fig. 1(a)]. The main process in a photocatalytic reaction starts with the absorption of photons by the photoanode and consequently the generation of an electron-hole pair (exciton). The second step consists of charge separation and migration of photogenerated carriers towards electrodes. Within this step, the morphological and electronic band structure of the semiconductor photoanode strongly affect light absorption, carrier separation and hence the overall photocatalytic performance of PEC devices [19,20].

Successively, electrons go through the external circuit and reach the cathode, where the final step of surface chemical reactions occur and hydrogen is produced [21]. A key process to increase the efficiency in PEC device is to improve the transport of photogenerated carriers to the electrodes where the reductive reaction leading to chemical fuel production, or the H_2 evolution reaction (HER) from H^+ (in acid) or H_2O (in the base) takes place [22].

A major hurdle to achieve this, is to facilitate the transport of photogenerated charges through the network of semiconductor

* Corresponding authors at: Institut National de la Recherche Scientifique, Centre Énergie, Matériaux et Télécommunications, 1650 Boul. Lionel Boulet Varennes, Québec, J3X 1S2, Canada.
** Corresponding author at: The State Key Laboratory & College of Physics, Qingdao University, No. 308 Ningxia Road, Qingdao, 266071, PR China.
E-mail addresses: gurpreet.selopal@emt.inrs.ca (G.S. Selopal), hgzhao@qdu.edu.cn (H. Zhao), rosei@emt.inrs.ca (F. Rosei).

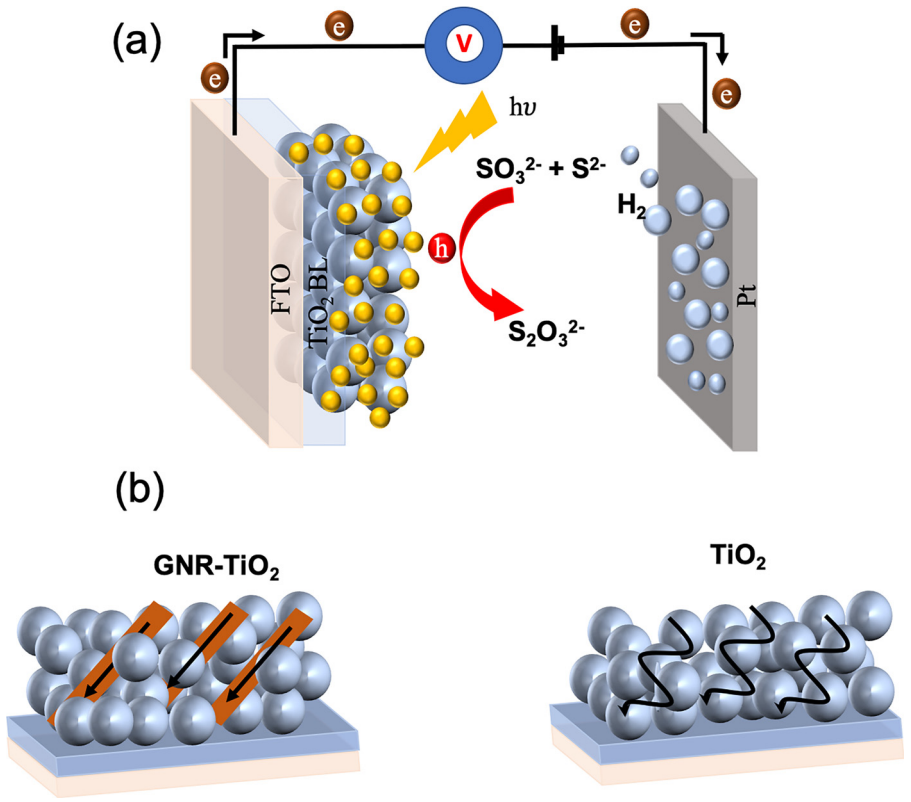

Fig. 1. (a) Schematic illustration of the working principle of PEC device for hydrogen generation. (b) Electron transport process in the mesoporous TiO_2 film with and without GNR. The arrows indicate the electron transfer process.

particles without any encounter between grain boundaries during the transit. To attain this, significant efforts have been devoted to design and synthesize different morphologies for the most commonly used wide band gap semiconductors (e.g. TiO_2 and ZnO), such as nanorods [23], nanotubes [24] and nanowires [25], to fabricate photoanodes with improved charge transport.

Due to their unique physical, chemical, electronic and mechanical properties, Graphene Nanoribbons (GNRs) are considered a promising one-dimensional (1D) nanomaterial [26–29] that may improve device performance. GNRs have been already employed with success in Li-ion batteries electrodes [30–32], in counter electrodes [33,34], and in wide bandgap semiconductor-based anodes [35] of DSSCs [36–38]. The challenge still remains to use this 1D network as a guide for providing direct low resistive pathways to these photogenerated electrons in semiconductor mesoporous films towards the fluorine doped tin oxide (FTO) conducting glass. The use of multi-walled carbon nanotubes (MWCNTs)-blended electrode with large band gap semiconductors for enhancing photoelectron transport has been recently proposed [39–41]. However, to the best of our knowledge, there are no reports on the use of GNRs, capable of focusing the electrons' random pathways into a more orientated directions, applied to PEC devices [42].

GNRs are capable of achieving high photocurrent and faster photoexcited electron transfer from the semiconductor to the liquid/solid interface through the 1D network of carbon, as in the case of hybrid GNRs-TiO_2 hybrid in DSSCs [35]. Electrons follow random paths after entering into the semiconductor nanoparticles anode and thus have a maximum probability to recombine due to intrinsic defects within the TiO_2 nanoparticle film, as shown in Fig. 1(b) [43]. Therefore, by addition of a small amount of GNRs, we can achieve a unidirectional flow of electrons for increasing charge transport efficiency [see Fig. 1(b)].

Here we report a simple, fast and cost-effective approach for the fabrication of GNRs-TiO_2 hybrid anodes sensitized with colloidal heterostructured quantum dots (QDs), to improve the performance of PEC cells for H_2 generation. The highest saturated photocurrent density of the PEC device based on GNRs-TiO_2/QDs hybrid photoanode reaches 5.51 mA/cm^2 (at 0.8 V RHE) under one sun illumination (AM 1.5 G, 100 mW/cm^2), which is 30% higher than the PEC device based on TiO_2/QDs photoanodes. This improvement is attributed to the enhanced electrons transport properties of GNRs-TiO_2/QDs hybrid photoanode. In addition, the long-term stability of the PEC device based on GNRs-TiO_2/QDs hybrid photoanode (0.02 wt%) is 15% better as compared to PEC based on TiO_2/QDs photoanode.

2. Experimental

2.1. Materials

Optically transparent fluorine doped SnO_2 (FTO) conducting substrates with sheet resistance 15 Ω/square were obtained from Xop Glass (Spain). The TiO_2 nano-oxide blocking layer solution was supplied from Solaronix. The mixed large and small mesoporous TiO_2 paste composed of 20 nm and up to 450 nm sized anatase particles (Code 18 NR-AO) were bought from Dyesol, Australia. Sulfur (100%), oleylamine (OLA) (technical grade, 70%), cadmium oxide (99%), cadmium nitrate tetra hydrate (≥99%), oleic acid (OA), Rhodamine 6 G and octadecene (ODE), selenium pellet (≥99.999%), trioctyl phosphine oxide (TOPO), trioctyl phosphine (TOP) (97%), hexane, zinc acetate dihydrate (98%), sodium sulfide nonahydrate (≥99.9%), sodiumsulfide (Na_2S), sodium hydroxide, sodium sulfite (Na_2SO_3), toluene, methanol, acetone, ethanol, dimethlyformamide (DMF) and isopropanol (IPA) were obtained from Sigma-Aldrich Inc.

2.2. GNR-TiO_2 hybrid film deposition

The GNR suspension was dispersed in DMF, for the exfoliation of carbon nanomaterials [44]. A thin and compact TiO_2 blocking layer was

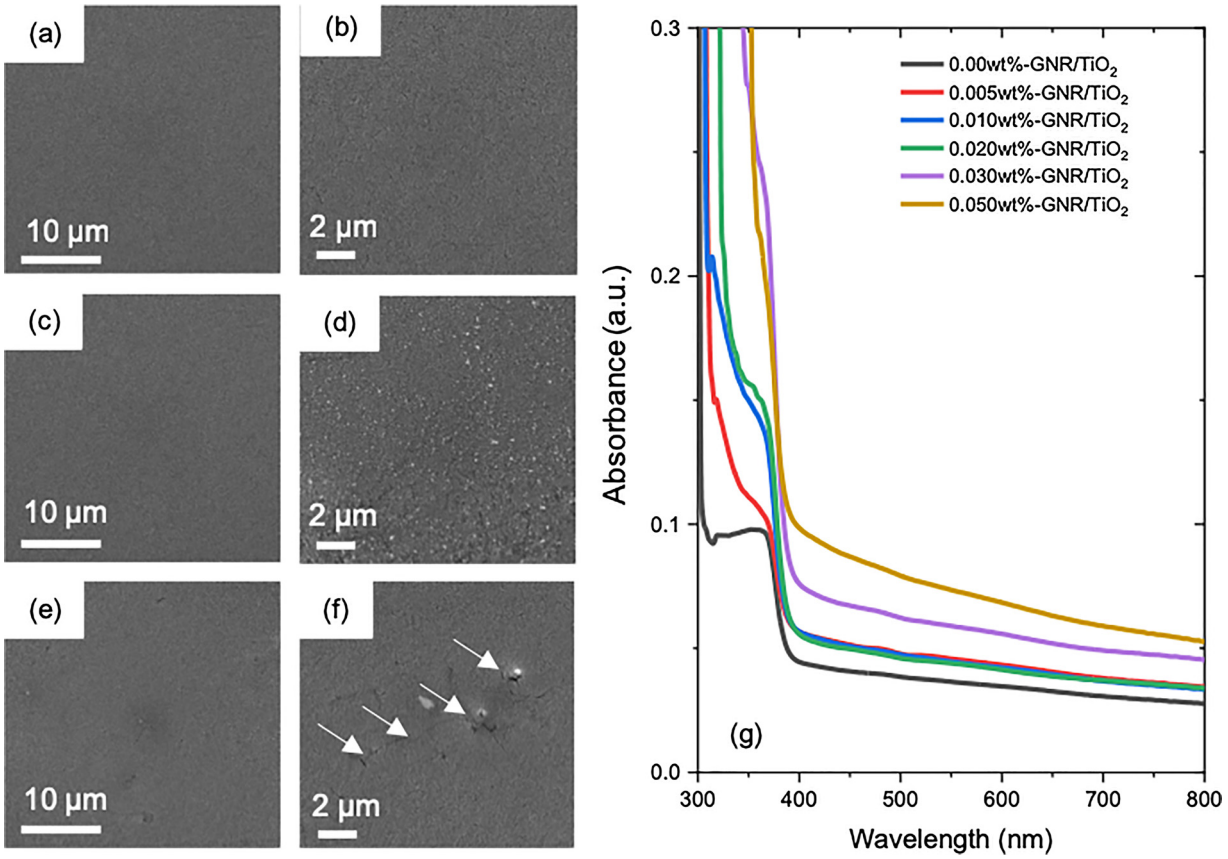

Fig. 2. SEM images of GNR-TiO_2 hybrid mesoporous films with different concentration of GNR: (a and b) 0.00 wt %; (c and d) 0.02 wt% and (e and f) 0.05 wt% at different magnifications. The presence of deep cracks at higher concentration of the GNR is highlighted by white arrows. A comparison of absorption spectra of GNR-TiO_2 hybrid mesoporous films deposited on transparent conducting oxide glass with different concentration of GNR (wt %).

deposited on ultrasonically cleaned FTO glass substrates by spin coating the Ti-Nanoxide solution at a speed of 6000 r.p.m. for 30 s. It was then annealed at 500 °C for 30 min under ambient atmosphere and left to cool down to room temperature. A suspension of GNRs was prepared by adding 6 mg of GNR in 15 ml of DMF and sonicated for 4 h. Subsequently, a double mesoporous layer was prepared by tape casting the hybrid GNR-TiO_2 paste containing different concentrations of GNRs suspension in TiO_2 nanoparticulate paste. Each layer was dried for 15 min under atmospheric conditions and then for 6 min at 120 °C. Then, all photoanodes were annealed at 500 °C for 30 min under ambient atmosphere. The film thickness was controlled through the number of layers of GNR-TiO_2 casted and measured by Alpha step 500 profilometer. After annealing, the photoanodes were characterized with UV–vis absorbance, scanning electron microscopy (SEM), transmission electron microscopy (TEM) and Raman spectroscopy. The final percentage weight of GNR in the TiO_2 photoanode was estimated using thermogravimetry and taking into account the photoanode weight after annealing [45].

2.3. EPD of the QDs on the TiO_2 and GNR-TiO_2 film and further ZnS coating

GNR-TiO_2 hybrid and TiO_2 films on FTO substrate were vertically immersed in the QDs toluene solution in such a way that the deposited films were facing each other. The distance between them was adjusted at around 1 cm and a direct current bias of 200 V was applied for 120 min. To wash off unabsorbed QDs after the EPD process, the samples were rinsed several times with toluene and dried with N_2 flow at room temperature. Prior to ZnS capping, photoanodes went through ligand exchange by applying 3 successive ionic layer adsorption and reaction (SILAR) cycles of methanolic solution cetyl-trimethyl ammonium bromide (CTAB) and toluene for 1 min dipping. After CTAB capping, 1 min dipping in methanol was applied to wash and remove the chemical residuals from the surface and then dried with N_2, finally 1 min dipping in toluene and dried with N_2 for one SILAR cycle. The ZnS capping layer was formed using the SILAR process as follows. In a typical SILAR deposition cycle, Zn^{2+} ions were deposited from a methanolic 0.1 M solution of $Zn(OAc)_2$. The sulfide precursor was 0.1 M solution of Na_2S in the mixture of methanol/water (1/1 v/v). A single SILAR cycle consisted of 1 min of dip-coating the TiO_2 working electrode into the cation precursors (Zn^{2+}), and subsequently into the anion solutions (S^{2-}). After each bath, the photoanode was thoroughly rinsed by immersing it in the corresponding solvent (methanol or mixed solution), respectively, to remove the chemical residuals from the surface and then drying with a N_2 gun. Two SILAR cycles were applied to form the capping ZnS layer.

2.4. Characterization

The PEC performance of the photoelectrodes was evaluated in a typical three-electrode configuration, consisting of a GNR-TiO_2/QDs hybrid mesoporous film as a working electrode, a Pt counter electrode, and a Ag/AgCl saturated reference electrode. An insulating epoxy resin was used to cover the sample's surface except for the active area, to avoid any direct contact between the electrolyte and the conducting back-contact and/or the connecting wire. Subsequently, the sample was fully immersed in the electrolyte containing 0.25 M Na_2S and 0.35 M Na_2SO_3 (pH ~ 13) as the sacrificial hole scavenger. All potentials, measured with respect to the reference electrode of Ag/AgCl during the PEC measurements, were converted to scale according to the following

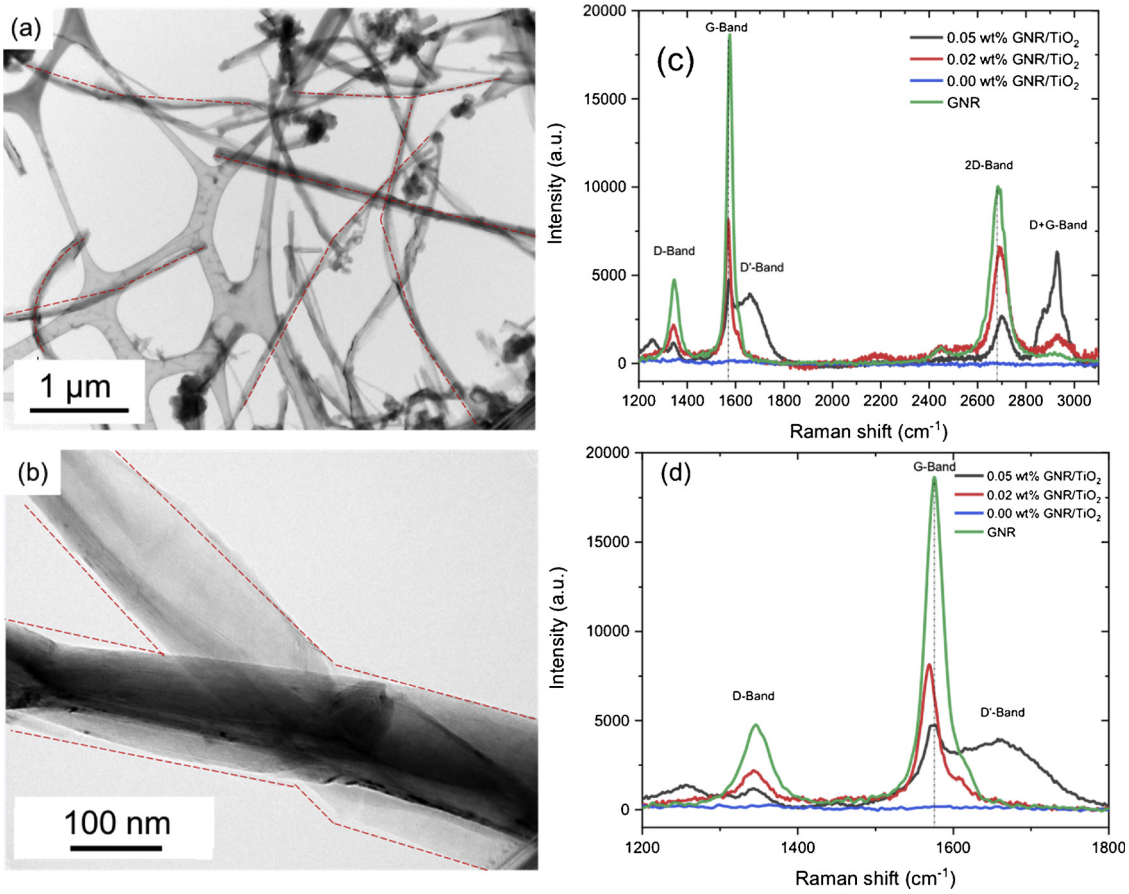

Fig. 3. (a) and (b) TEM images of GNRs (highlighted by red-dotted line) supported on Cu grid at different magnification. Raman mapping of the GNR (green line), TiO_2 (blue line), GNR-TiO_2 (red line) composite photoanode with GNR = 0.02 wt% and GNR-TiO_2 (black line) composite photoanode with GNR = 0.05 wt% (For interpretation of the references to colour in this figure legend, the reader is referred to the web version of this article).

equation $V_{RHE} = V_{Ag/AgCl} + 0.197V + pH * (0.059)$. The photo response was measured by using a sun simulator (Sciencetech SLB-300 A) under one sun simulated sunlight. The sample was placed at a distance of two cm from the lamp case (seven cm far from the actual bulb). Prior to each measurement, light intensity monitored using a silicon reference cell and adjusted to 100 mW/cm^2. All the current versus potential measurements were carried out at a 20 mV/s sweep rate. Electrochemical impedance spectroscopy (EIS) was carried under dark conditions by using a SOLARTRON 1260 A Impedance/Gain-Phase Analyzer by applying open circuit conditions with a test recorded at a frequency of 300 kHz to 1 Hz, and the AC signal was 1 mV rms in amplitude. All the impedance measurements were analyzed using an appropriate equivalent circuit model with Gamry software (Version 7.5, Echem Analyst).

3. Results and discussion

3.1. Structural and morphological characterization of GNR-TiO_2 hybrid anode

SEM images of the bare TiO_2 and GNR-TiO_2 hybrid mesoporous anodes with different concentrations of GNRs at different magnification are shown in Fig. 2(a)–(f). SEM images of bare TiO_2 mesoporous film confirm the formation crack-free and porous film [see Fig. 2(a) and (b)]. Fig. 2(c) and (d) displays SEM images of GNR-TiO_2 hybrid mesoporous film with an optimized concentration of GNR (0.02 wt%). However, it is very hard to identify the presence of GNRs in the hybrid mesoporous film due to the low concentration of GNR and complete coverage of GNR by TiO_2 nanoparticles as generally observed for the similar carbonaceous-TiO_2 hybrid system [41,46]. SEM images of GNR-TiO_2 hybrid mesoporous film with the highest concentration of GNR (0.05 wt%) exhibits a series of deep cracks [Fig. 2(e) and (f)], which are not observed in bare TiO_2 and GNR-TiO_2 hybrid mesoporous film with an optimized concentration of GNR (0.02 wt%).

The presence of these cracks with high loading of GNR (0.05 wt%) in the GNR-TiO_2 hybrid anode, hinder the efficient transport of electrons within the photoanode by trapping inside the anode. In addition, these cracks act as recombination sites for electrolyte and back transfer electrons (electrolyte/FTO). This may reduce the device's overall functional performance, confirmed also by photocurrent density measurements of PEC based on respective photoanodes (more details reported in PEC measurement section).

The transparency of the GNR-TiO_2 hybrid mesoporous film in the UV–vis region changes with different content of GNRs. Fig. 2(g) displays the variation of absorption spectra of GNR-TiO_2 hybrid mesoporous film with GNRs concentration. The transparency of GNR-TiO_2 hybrid mesoporous film with GNR content below 0.02 wt% is comparable to bare TiO_2 and absorption peak positions are close to each other, since they both show a drastically increased absorption intensity at 400 nm, corresponding to the intrinsic band gap of anatase TiO_2. However, further increasing the content of GNR (0.03–0.05 wt%) in the hybrid film reduces its transparency. The UV–vis spectrum of GNR-TiO_2 hybrid film (0.03-0.05 wt%) shows a stronger absorption in the range of 400–800 nm than bare TiO_2 and GNR-TiO_2 hybrid (GNR less than 0.02 wt%) and is consistent with the reported literature on carbonaceous-TiO_2 hybrid film [47–52]. There is an obvious correlation between the GNRs content and the UV–vis spectrum change, that can be attributed to the GNRs sheets on the surface of TiO_2. The absorption of

GNR-TiO_2 hybrid anode remains unaltered, when the mass amount of GNR is less than 0.02 wt%, probably due to the chemical monolayer adsorption. Once the monolayer coverage becomes saturated, further addition of GNRs tends to form multilayers, which will evolve into clusters that reduce the transparency [53,54]. Therefore, direct light absorption by the GNRs results in a loss of part of the radiation available for exciton generation, which in turn worsens the device's overall performance.

TEM images of GNRs (highlighted by red-dotted lines) supported on a Cu grid are shown at different scales in Fig. 3(a) and (b). The micrographs show that GNRs used in this work are a few-layers graphene, which is further confirmed by Raman spectroscopy measurements.

Fig. 3(c) and (d) displays the spectra of representative samples of GNR-TiO_2 hybrid mesoporous film at 0.02 and 0.05 wt%, and a Raman spectrum of GNR. The details in Fig. 3(d) consists of two dominant characteristic Raman features, the so-called D-band and G-band at 1346 cm^{-1} and 1576 cm^{-1} respectively for GNR, 1342 cm^{-1} and 1569 cm^{-1} respectively for 0.02 wt% hybrid GNR-TiO_2, 1342 cm^{-1} and 1575 cm^{-1} respectively for 0.05 wt% hybrid GNR-TiO_2 [48]. As the amount of GNRs is increased from 0.02 to 0.05 wt% (I_D /I_G = 0.28 and I_D /I_G = 0.42 respectively) into the TiO_2, the I_D/I_G ratio increases as well by 0.14 point. This increased ratio confirms that the higher amount of GNRs introduce more defects [55]. In addition, the presence of the disorder-induced D'-band at the right side of the G-band can be also confirmed, which is activated by long-range defects such as charged impurities absorbed on the GNR sheets [56]. This D'-band evolves from a small overlap into wider and more prominent and distinct peaks (from 1608 cm^{-1} for 0.02 wt% to 1659 cm^{-1} for 0.05 wt%).

Besides the overall decrease of the D-band and the 2D-band [55] (both only active in the vicinity of point defects) as we increase the amount of GNRs, the 2D-band shown in Fig. 3(c) reveals a peak shift into higher wavenumbers as well as an asymmetric shape with a full width half maxima (FWHM) of ~52.8–57.5 cm^{-1} when embedded in the mesoporous film. This supports the hypothesis that the GNRs in the hybrid film is composed of few layers GNRs, as much as the pristine GNR (FWHM (2D) of 61 cm^{-1}) [57]. The decrease in the intensity of the G-band with further increase in GNRs concentration (0.03–0.05 wt %), suggests that the quality of GNRs in the TiO_2 matrix is diminished. A further confirmation of lower GNR quality can be seen in the defect activated D'-bands [58–60] and D + G-bands [61] whose intensities and FWHM steadily increases and the I_D/I_G ratio (indicating structural defects and disorder in the carbon network) also increases from 0.36 to 0.42 for bare and 0.05 wt% GNRs samples respectively. These trends show that the increased amount of GNRs gradually reduces the overall quality of the GNRs inside the TiO_2 film.

3.2. Structural and optical characterization of QDs

CdSe QDs were first synthesized via a hot injection approach as reported elsewhere [62]. Then a CdS shell was further grown by SILAR [63] at 240 °C under N_2 flow. The diameter of starting CdSe core QDs is around 3.30 ± 0.29 nm with uniform size distribution (< 10%). The increased size of QDs after the six CdS shells growth, was confirmed by TEM analysis (see Fig. 4(a). The average size of CdSe/6CdS QDs is 7.24 ± 0.46 nm with an average shell thickness (H) of 1.96 nm (estimated from TEM images). The high crystallinity of as-prepared QD is confirmed by HRTEM images, in which lattice fringes of QDs is clearly visible (inset of Fig. 4(a).

The optical properties of as-synthesized CdSe/$(CdS)_6$ core/shell QDs in toluene are shown in Fig. 4(b)–(e). The first absorption excitonic peak is observed at 591 nm with broad absorption spectra range from UV to the visible region [see Fig. 4(b)] [64]. This broad absorption feature of the core/shell QDs may be due to carrier delocalization into the shell region. PL spectra of as-synthesized CdSe/$(CdS)_6$ core/shell QDs in toluene are shown in Fig. 4(c). The PL peak of CdSe/$(CdS)_6$ core/shell QDs is centered at 605 nm.

Carrier dynamic behavior of the CdSe/$(CdS)_6$ core/shell QDs after coupling with semiconductor metal oxide was studied by transient PL spectroscopy technique. The electron lifetime and electron transfer rate of QDs deposited on TiO_2 or ZrO_2 mesoporous films were measured under an excitation wavelength of λ = 444 nm. All PL decay curves were well fitted using a three-stage exponential decay. The intensity-weighted average lifetime (< τ >) is calculated by using the following equation:

$$<\tau> = \frac{a_1\tau_1^2 + a_2\tau_2^2 + a_3\tau_3^2}{a_1\tau_1 + a_2\tau_2 + a_3\tau_3} \quad (1)$$

Where a_x (x = 1–3) are the fitting coefficients of the PL decay and τ_x (x = 1–3) are the characteristic lifetimes, respectively. PL decay is faster in case of QDs anchored with TiO_2 than QDs with ZrO_2, which confirms an efficient electron transfer from QDs to the TiO_2 (Fig. 4(d) and (e)). This is mainly due to the difference in electronic band alignment of ZrO_2 (position of conduction band (CB) edge) and TiO_2, which in case of ZrO_2 is not suitable for electron transfer from QDs. The calculated average electron lifetime values for QDs anchored to the TiO_2 mesoporous film is 23 ± 2 ns, whereas for QDs anchored to the ZrO_2 mesoporous film is 25 ± 1 ns, values comparable to the one in literatures [65]. The difference between the average lifetime values gives the electron transfer rate (K_{et}), which is 0.9 ± 0.2 × 10^7/s.

3.3. PEC measurements

We applied GNR-TiO_2 hybrid mesoporous films with different content of GNR sensitized with colloidal CdSe/$(CdS)_6$ core/shell QDs as working electrodes to fabricate a PEC device. A bare TiO_2 mesoporous film sensitized with colloidal CdSe/$(CdS)_6$ core/shell QDs was also applied as a working electrode and considered as a reference to highlight the effect of GNR. PEC measurements were performed under dark, continuous and chopped illumination (AM 1.5 G, 100 mW·cm^{-2}) by using a typical three-electrode configuration system. The current density vs applied potential curves of GNR-TiO_2/QDs hybrid photoanode with different concentration of GNR and TiO_2/QDs photoanode as a reference are shown in Fig. 5(a)–(e).

The photocurrent density for all PEC devices varies with the different content of GNR in the TiO_2 mesoporous film. The variation of saturated photocurrent density values versus the concentrations of GNR in the hybrid photoanode at 0.8 V_{RHE} is summarized in Fig. 5(f) and corresponding values are reported in Table 1. In brief, at 0.8 V vs RHE, the highest saturated photocurrent density of the PEC system based on bare TiO_2/QDs photoanode is 4.21 mA/cm^2 under one sun illumination. With the addition 0.01 wt% of GNR in TiO_2, the saturated photocurrent density increases to 4.51 mA/cm^2 under one sun illumination, then reaches to maximum value of 5.51 mA/cm^2 at 0.02 wt% of GNR content, which is 30% higher than that of a PEC system based on the bare TiO_2/QDs photoanode. This improvement in photocurrent density with the addition of 0.02 wt% GNR in the hybrid photoanode based PEC cells is mainly attributed to enhanced electron transport and reduced charge transfer resistance (see more details in EIS section).

For further increases in the concentration of GNRs, the photocurrent density reduces from 5.51 to 4.65 mA/cm^2 (0.03 wt%) and 3.85 mA/cm^2 (0.05 wt%) as mentioned previously. This is mainly due to the detrimental effect of the high concentration of GNRs such as crack formation, which acts as recombination centers during carrier transport and also due to the reduced optical transparency of the hybrid photoanode.

3.4. Electrochemical impedance spectroscopy analysis

To fully understand the mechanism behind the improved performance for an optimal amount of GNRs and explore the electron transfer kinetic mechanism, we performed electrochemical impedance spectra

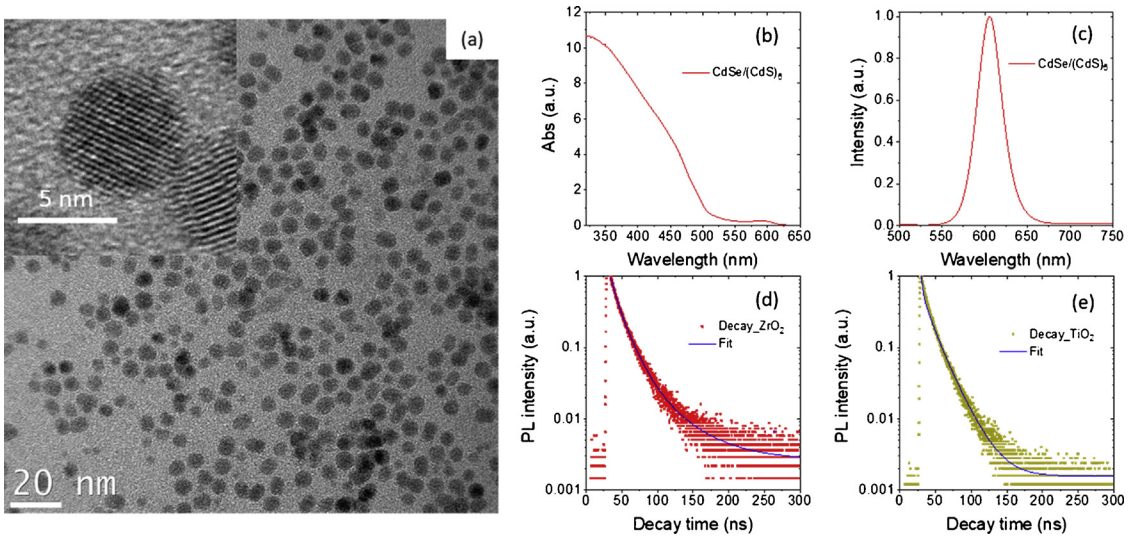

Fig. 4. (a) TEM image of CdSe/$(CdS)_6$ core/shell QDs, the inset shows the HR-TEM image. Optical properties of QDs: (b) Absorption spectrum in UV–vis region of as-synthesized CdSe/$(CdS)_6$ core/shell QDs in toluene; (c) PL spectra of respective QDs in toluene. Transient PL curves of CdSe/$(CdS)_6$ core/shell QDs: (d) Deposited onto ZrO_2 mesoporous film; (b) Deposited onto and TiO_2 mesoporous film. The excitation wavelength is $\lambda = 444$ nm.

(EIS) [66]. A three-electrode system was employed with the bare TiO_2 or GNR-TiO_2 photoanodes as working electrode, Ag/AgCl as reference electrode and a platinum foil as counter electrode.

The Nyquist plot reported in Fig. 6 presents a small semicircle at high frequencies and a large one at low frequencies. The arc at low frequency corresponds to charge transfer resistance (R_{ct}) and indicates the charge transfer is the dominant process at this stage [67,68]. A small R_{ct} indicates a higher charge transfer and an improved separation of electron/hole pairs [67]. As visible in the Nyquist plot and in the table, the addition of an optimum amount of GNRs in the TiO_2 matrix

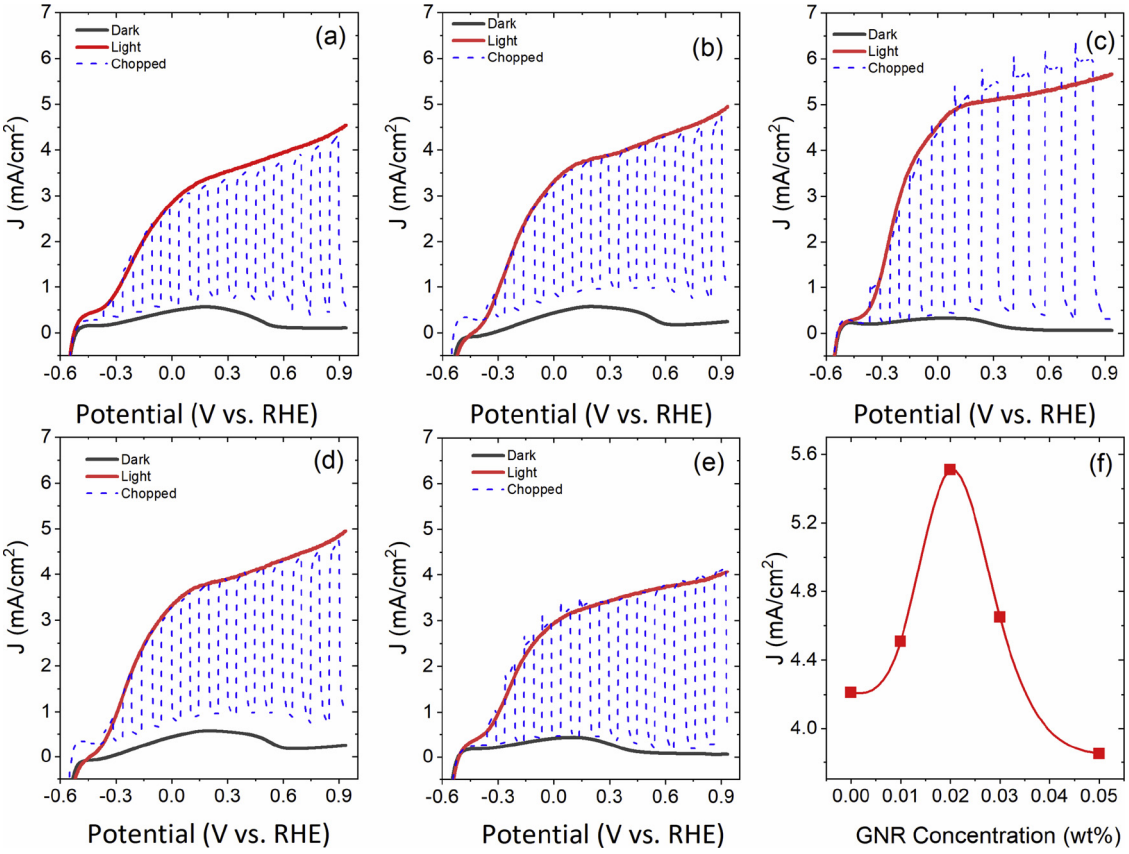

Fig. 5. Photocurrent density-potential curves of PEC devices based on QDs sensitized GNR-TiO_2 hybrid photoanodes under dark (black solid line), chopped (dotted blue line) and continuous illumination (AM 1.5 G, 100 mW/cm^2) (red solid line) with different concentration of GNR: (a) 0.00 wt%; (b) 0.01 wt%; (c) 0.02 wt%; (d) 0.03 wt%; and (e) 0.05 wt%. (f) Variation of photocurrent density of PEC devices based on QDs sensitized GNR-TiO_2 hybrid photoanodes with different content of GNR at 0.8 V vs RHE under on sun illumination (AM 1.5 G, 100 mW/cm^2) (For interpretation of the references to colour in this figure legend, the reader is referred to the web version of this article).

Table 1
Comparison of photocurrent density at 0.8 V vs RHE under one sun illumination (AM 1.5 G, 100 mW·cm^{-2}) of PEC devices based on GNR-TiO_2/QDs hybrid photoanodes with different concentration of GNR (wt%).

GNR (wt %)	J (mA/cm^2)
0	4.21
0.01	4.51
0.02	5.51
0.03	4.65
0.05	3.85

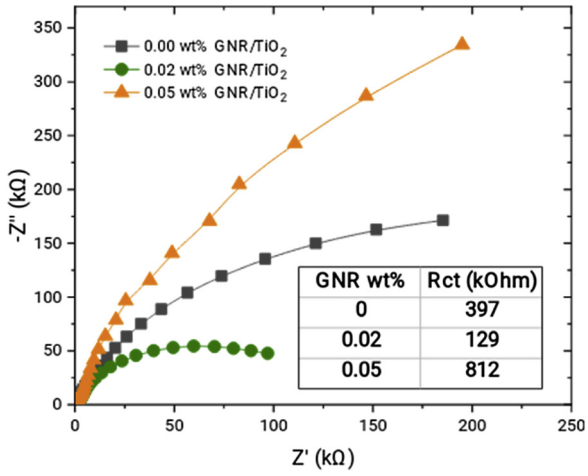

Fig. 6. The Nyquist plot of PEC devices based on GNR-TiO_2/QDs hybrid photoanodes with different concentration of GNR (wt%): Black square (0.0 wt%); Green circle (0.02 wt%) and Orange upper triangle (0.05 wt%). Inset table displays the variation of charge transfer resistance (k ohm) with GNRs concentration (wt%) (For interpretation of the references to colour in this figure legend, the reader is referred to the web version of this article).

leads to a decrease in the R_{ct}, indicating an improved charge transfer for the best photoanode. Instead, when the GNR amount is increased, the charge transfer kinetics becomes slower, thereby reducing the current generated by the cell. This phenomenon can probably be attributed to the agglomeration of carbon nanostructures, as previously observed [35,41].

3.5. Long-term stability measurements

The long-term stability measurements were carried under continuous one sun illumination (AM 1.5 G, 100 mW·cm^{-2}). We fabricated two types of PEC devices based on TiO_2/QDs and the best PEC performing hybrid GNRs-TiO_2/QDs (0.02 wt%) to highlight the effect of GNRs addition on long-term stability. A systematic comparison of normalized photocurrent density of PEC devices based on TiO_2/QDs and GNR-TiO_2/QDs (0.02 wt%) under continuous one sun illumination as a function of time is shown in Fig. 7. The PEC device based on hybrid GNRs-TiO_2/QDs maintains ~65% of the initial photocurrent density after 7200 s of continuous one sun illumination, whereas in case of the PEC device based on TiO_2/QDs photoanode maintains only ~50% of its initial photocurrent density. In both devices, all components are the same, so this difference in long-term stability of PEC devices with and without GNRs, is mainly attributed to the presence of GNRs in the TiO_2 mesoporous film, which acts as UV light absorber and simultaneously facilitates the removal of the charges, in turn improving long-term stability [69–71].

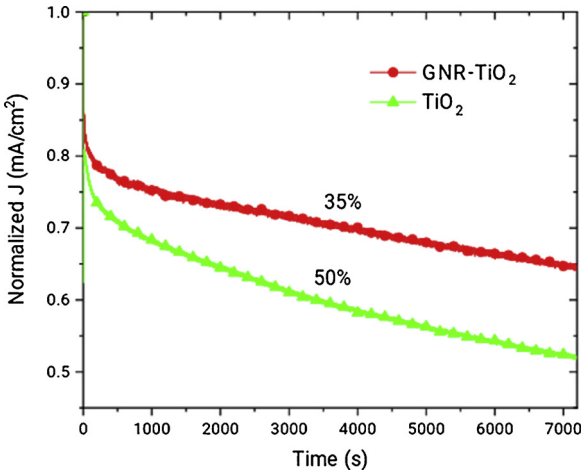

Fig. 7. Comparison of normalized current density (mW·cm^{-2}) versus time for PEC devices based on GNR-TiO_2/QDs (red circle) and TiO_2/QDs (green upper triangle) photoanodes at 0.6 V (versus RHE) under one sun continuous illumination (AM 1.5 G, 100 mW·cm^{-2}) for 7200 s. (For interpretation of the references to colour in this figure legend, the reader is referred to the web version of this article).

4. Conclusions and perspectives

In summary, we prepared GNR-TiO_2 hybrid anodes with different concentrations (wt.%) of GNRs. The structural and optical properties of GNRs-TiO_2 hybrid anodes were characterized using UV–vis, SEM and Raman spectroscopy. GNRs-TiO_2 hybrid anodes were sensitized with a CdSe/$(CdS)_6$ colloidal core/shell QDs. The optimized concentration of GNRs (0.02 wt %) in the TiO_2 mesoporous film sensitized with CdSe/$(CdS)_6$ colloidal core/shell QDs, yielded the highest photocurrent density of 5.51 mA/cm^2 (at 0.08 V vs RHE) under one sun illumination (AM 1.5 G, 100 mW·cm^{-2}), which is 30% higher than the control device. This demonstrates that a small amount of GNRs (0.02 wt%) dispersed in TiO_2 leads to improved electron transport (reducing the R_{ct}) due to the directional path offered by GNRs to photoinjected electrons towards FTO. Furthermore, the PEC device based on TiO_2-GNRs/QDs hybrid photoanode shows better long-term stability as compared to TiO_2/QDs photoanode. Our results offer a simple and low-cost approach to improve the performance of PEC devices as well as the possibility to use other low dimensional carbonaceous materials to boost the efficiency of PEC devices. Future directions will focus on the application of functionalized GNRs in TiO_2 mesoporous films with best performing heterostructured colloidal QDs, to realize high efficiency and long-term stable PEC devices.

Acknowledgements

We acknowledge funding from the Natural Science and Engineering Research Council of Canada (NSERC), the Canada Foundation for Innovation (CFI) for infrastructure support and its operating funds. F.R. is also grateful to the government of China for a Chiang Jiang scholar short-term award and Sichuan province for a short-term 1000 talent plan award. F.R. also acknowledges IFFS/UESTC for partial funding of this work. G.S.S. acknowledges the UNESCO Chair MATECSS for a PDF Excellence Scholarship and funding from the IFFS/UESTC and the Postdoctoral Science Foundation of China. M.M. is thankful to FRQNT for a Ph.D scholarship (B2X). F.R. is grateful to the Canada Research Chairs program for funding and partial salary support. H.G. Zhao acknowledges start-up funds from Qingdao University and funding from the Natural Science Foundation of Shandong Province (ZR2018MB001).

References

[1] S. Singh, S. Jain, V. Ps, A.K. Tiwari, M.R. Nouni, J.K. Pandey, S. Goel, Hydrogen: a sustainable fuel for future of the transport sector, Renew. Sustain. Energy Rev. 51 (2015) 623–633, https://doi.org/10.1016/j.rser.2015.06.040.

[2] A.M. Abdalla, S. Hossain, O.B. Nisfindy, A.T. Azad, M. Dawood, A.K. Azad, Hydrogen production, storage, transportation and key challenges with applications: a review, Energy Convers. Manage. 165 (2018) 602–627, https://doi.org/10.1016/J.ENCONMAN.2018.03.088.

[3] F. Mueller-Langer, E. Tzimas, M. Kaltschmitt, S. Peteves, Techno-economic assessment of hydrogen production processes for the hydrogen economy for the short and medium term, Int. J. Hydrogen Energy 32 (2007) 3797–3810, https://doi.org/10.1016/J.IJHYDENE.2007.05.027.

[4] L. Barreto, A. Makihira, K. Riahi, The hydrogen economy in the 21st century: a sustainable development scenario, Int. J. Hydrogen Energy 28 (2003) 267–284, https://doi.org/10.1016/S0360-3199(02)00074-5.

[5] W.C. Lattin, V.P. Utgikar, Transition to hydrogen economy in the United States: a 2006 status report, Int. J. Hydrogen Energy 32 (2007) 3230–3237, https://doi.org/10.1016/J.IJHYDENE.2007.02.004.

[6] R. Ramachandran, R.K. Menon, An overview of industrial uses of hydrogen, Int. J. Hydrogen Energy 23 (1998) 593–598, https://doi.org/10.1016/S0360-3199(97)00112-2.

[7] N. Eliaz, D. Eliezer, D.L. Olson, Hydrogen-assisted processing of materials, Mater. Sci. Eng. A. 289 (2000) 41–53, https://doi.org/10.1016/S0921-5093(00)00906-0.

[8] D. Eliezer, N. Eliaz, O.N. Senkov, F.H. Froes, Positive effects of hydrogen in metals, Mater. Sci. Eng. A. 280 (2000) 220–224, https://doi.org/10.1016/S0921-5093(99)00670-X.

[9] H.L. Tuller, Solar to fuels conversion technologies: a perspective, Mater. Renew. Sustain. Energy 6 (2017) 3, https://doi.org/10.1007/s40243-017-0088-2.

[10] O. Inganäs, V. Sundström, Solar energy for electricity and fuels, Ambio 45 (2016) 15–23, https://doi.org/10.1007/s13280-015-0729-6.

[11] P.V. Kamat, J. Bisquert, Solar fuels. Photocatalytic hydrogen generation, J. Phys. Chem. C 117 (2013) 14873–14875, https://doi.org/10.1021/jp406523w.

[12] R.J. Cogdell, A.T. Gardiner, P.I. Molina, L. Cronin, The use and misuse of photosynthesis in the quest for novel methods to harness solar energy to make fuel, Philos. Trans. R. Soc. A Math. Phys. Eng. Sci. 371 (2013) 20110603, , https://doi.org/10.1098/rsta.2011.0603.

[13] T.R. Cook, D.K. Dogutan, S.Y. Reece, Y. Surendranath, T.S. Teets, D.G. Nocera, Solar energy supply and storage for the legacy and nonlegacy worlds, Chem. Rev. 110 (2010) 6474–6502, https://doi.org/10.1021/cr100246c.

[14] K.-V. Peinemann, S.P. Nunes, Membrane technology, Membranes for Energy Conversion vol. 2, Wiley-VCH, 2008, https://www.wiley.com/en-ca/Membranes+for+Energy+Conversion-p-9783527622245.

[15] M.A. Pellow, C.J.M. Emmott, C.J. Barnhart, S.M. Benson, Hydrogen or batteries for grid storage? A net energy analysis, Energy Environ. Sci. 8 (2015) 1938–1952, https://doi.org/10.1039/c4ee04041d.

[16] B. You, Y. Sun, Innovative strategies for electrocatalytic water splitting, Acc. Chem. Res. 51 (2018), https://doi.org/10.1021/acs.accounts.8b00002 acs.accounts.8b00002.

[17] L. Dai, D.W. Chang, J.-B. Baek, W. Lu, Carbon nanomaterials for advanced energy conversion and storage, Small 8 (2012) 1130–1166, https://doi.org/10.1002/smll.201101594.

[18] P. Zhang, T. Wang, J. Gong, Current mechanistic understanding of surface reactions over water-splitting photocatalysts, Chem 4 (2018) 223–245, https://doi.org/10.1016/j.chempr.2017.11.003.

[19] M.G. Walter, E.L. Warren, J.R. McKone, S.W. Boettcher, Q. Mi, E.A. Santori, N.S. Lewis, Solar water splitting cells, Chem. Rev. 110 (2010) 6446–6473, https://doi.org/10.1021/cr1002326.

[20] Y. Tachibana, L. Vayssieres, J.R. Durrant, Artificial photosynthesis for solar water-splitting, Nat. Photon. 6 (2012) 511–518, https://doi.org/10.1038/nphoton.2012.175.

[21] A. Kudo, Y. Miseki, Heterogeneous photocatalyst materials for water splitting, Chem. Soc. Rev. 38 (2009) 253–278, https://doi.org/10.1039/b800489g.

[22] S. Dahl, I. Chorkendorff, Towards practical implementation, Nat. Mater. 11 (2012) 100–101, https://doi.org/10.1038/nmat3233.

[23] B. Sun, T. Shi, Z. Peng, W. Sheng, T. Jiang, G. Liao, Controlled fabrication of Sn/TiO_2 nanorods for photoelectrochemical water splitting, Nanosc. Res. Lett. 8 (2013) 462, https://doi.org/10.1186/1556-276X-8-462.

[24] S. Palmas, A. Da Pozzo, F. Delogu, M. Mascia, A. Vacca, G. Guisbiers, Characterization of TiO_2 nanotubes obtained by electrochemical anodization in organic electrolytes, J. Power Sources 204 (2012) 265–272, https://doi.org/10.1016/J.JPOWSOUR.2012.01.007.

[25] S. Hoang, S. Guo, N.T. Hahn, A.J. Bard, C.B. Mullins, Visible light driven photoelectrochemical water oxidation on nitrogen-modified TiO_2 nanowires, Nano Lett. 12 (2012) 26–32, https://doi.org/10.1021/nl2028188.

[26] A. Akbari-Sharbaf, M.G. Cottam, G. Fanchini, A combined theoretical-experimental investigation of paramagnetic centres in chemically exfoliated graphene nanoribbons, J. Appl. Phys. 114 (2013) 24309, https://doi.org/10.1063/1.4813142.

[27] E. Kozma, D. Kotowski, M. Catellani, S. Luzzati, M. Cavazzini, A. Bossi, S. Orlandi, F. Bertini, Design of perylene diimides for organic solar cell: effect of molecular steric hindrance and extended conjugation, Mater. Chem. Phys. 163 (2015) 152–160, https://doi.org/10.1016/j.matchemphys.2015.07.025.

[28] G. Bottari, G. De La Torre, D.M. Guldi, T. Torres, Covalent and noncovalent phthalocyanine–carbon nanostructure systems: synthesis, photoinduced electron transfer, and application to molecular photovoltaics, Chem. Rev. 110 (2010) 6768–6816, https://doi.org/10.1021/cr900254z.

[29] H. Imahori, T. Umeyama, S. Ito, Large π-aromatic molecules as potential sensitizers for highly efficient dye-sensitized solar cells, Acc. Chem. Res. 42 (2009) 1809–1818, https://doi.org/10.1021/ar900034t.

[30] R. Tian, W. Wang, Y. Huang, H. Duan, Y. Guo, H. Kang, H. Li, H. Liu, 3D composites of layered MoS_2 and graphene nanoribbons for high performance lithium-ion battery anodes, J. Mater. Chem. A 4 (2016) 13148–13154, https://doi.org/10.1039/C6TA04331C.

[31] S.J. Lee, J.-Y. Kim, H.P. Kim, D. Kim, W.J. da Silva, F.K. Schneider, A.R. Bin Mohd Yusoff, J. Jang, An organic photovoltaic featuring graphene nanoribbons, Chem. Commun. 51 (2015) 9185–9188, https://doi.org/10.1039/C5CC01375E.

[32] S.W. Chong, C.W. Lai, S.B. Abd Hamid, Controllable electrochemical synthesis of reduced graphene oxide thin-film constructed as efficient photoanode in dye-sensitized solar cells, Materials (Basel) 9 (2016) 69, https://doi.org/10.3390/ma9020069.

[33] M. Liu, Y. Song, S. He, W.W. Tjiu, J. Pan, Y.Y. Xia, T. Liu, Nitrogen-doped graphene nanoribbons as efficient metal-free electrocatalysts for oxygen reduction, ACS Appl. Mater. Interfaces 6 (2014) 4214–4222, https://doi.org/10.1021/am405900r.

[34] X. Meng, C. Yu, X. Song, Y. Liu, S. Liang, Z. Liu, C. Hao, J. Qiu, Nitrogen-doped graphene nanoribbons with surface enriched active sites and enhanced performance for dye-sensitized solar cells, Adv. Energy Mater. 5 (2015) 1500180, , https://doi.org/10.1002/aenm.201500180.

[35] R. Akilimali, G.S. Selopal, D. Benetti, I. Serrano-Esparza, P.A. Algarabel, J.M. De Teresa, Z.M. Wang, B. Stansfield, H. Zhao, F. Rosei, Hybrid TiO_2 -graphene nanoribbon photoanodes to improve the photoconversion efficiency of dye sensitized solar cells, J. Power Sources 396 (2018) 566–573, https://doi.org/10.1016/j.jpowsour.2018.06.044.

[36] N. Mohanty, D. Moore, Z. Xu, T.S.S. Sreeprasad, A. Nagaraja, A.A. Rodriguez, V. Berry, Nanotomy-based production of transferable and dispersible graphene nanostructures of controlled shape and size, Nat. Commun. 3 (2012) 844, https://doi.org/10.1038/ncomms1834.

[37] C. Soldano, S. Talapatra, S. Kar, Carbon Nanotubes and Graphene Nanoribbons: Potentials for Nanoscale Electrical Interconnects, (2013), https://doi.org/10.3390/electronics2030280.

[38] A. Dimiev, W. Lu, K. Zeller, B. Crowgey, L.C. Kempel, J.M. Tour, Low-loss, high-permittivity composites made from graphene nanoribbons, ACS Appl. Mater. Interfaces 3 (2011) 4657–4661, https://doi.org/10.1021/am201071h.

[39] U. Mehmood, I.A. Hussein, K. Harrabi, M.B. Mekki, S. Ahmed, N. Tabet, Hybrid TiO_2–multiwall carbon nanotube (MWCNTs) photoanodes for efficient dye sensitized solar cells (DSSCs), Sol. Energy Mater. Sol. Cells 140 (2015) 174–179, https://doi.org/10.1016/j.solmat.2015.04.004.

[40] Y.-C. Shih, C.-W. Yeh, K.-F. Lin, Photovoltaic performance enhancement of dye-sensitized solar cells by incorporating poly(sodium-4-styrenesulfonate)-physisorbed MWCNTs into photoelectrode, Mater. Chem. Phys. 171 (2016) 352–358, https://doi.org/10.1016/j.matchemphys.2016.01.028.

[41] D. Benetti, K.T. Dembele, J. Benavides, H. Zhao, S. Cloutier, I. Concina, A. Vomiero, F. Rosei, Functionalized multi-wall carbon nanotubes/TiO_2 composites as efficient photoanodes for dye sensitized solar cells, J. Mater. Chem. C 4 (2016) 3555–3562, https://doi.org/10.1039/C6TC00800C.

[42] X. Huang, C. Tan, Z. Yin, H. Zhang, 25th anniversary article: hybrid nanostructures based on two-dimensional nanomaterials, Adv. Mater. 26 (2014) 2185–2203, https://doi.org/10.1002/adma.201304964.

[43] P.V. Kamat, Meeting the clean energy demand: nanoestructure architectures for solar energy conversion, Phys. Chem. 392 (2007) 2834–2860, https://doi.org/10.1002/adma.200902096.

[44] M. Quintana, M. Prato, Supramolecular aggregation of functionalized carbon nanotubes, Chem. Commun. (2009) 6005, https://doi.org/10.1039/b915126e.

[45] K.T. Dembele, G.S. Selopal, R. Milan, C. Trudeau, D. Benetti, A. Soudi, M.M. Natile, G. Sberveglieri, S. Cloutier, I. Concina, F. Rosei, A. Vomiero, Graphene below the percolation threshold in TiO_2 for dye-sensitized solar cells, J. Mater. Chem. A 3 (2014) 2580–2588, https://doi.org/10.1039/C4TA04395B.

[46] K.T. Dembele, R. Nechache, L. Nikolova, A. Vomiero, C. Santato, S. Licoccia, F. Rosei, Effect of multi-walled carbon nanotubes on the stability of dye sensitized solar cells, J. Power Sources 233 (2013) 93–97, https://doi.org/10.1016/j.jpowsour.2013.01.075.

[47] L. Zhang, Y. Wang, T. Xu, S. Zhu, Y. Zhu, Surface hybridization effect of C60 molecules on TiO_2 and enhancement of the photocatalytic activity, J. Mol. Catal. A Chem. 331 (2010) 7–14, https://doi.org/10.1016/J.MOLCATA.2010.07.015.

[48] S. Hu, F. Li, Z. Fan, The property and photocatalytic performance comparison of graphene, carbon nanotube, and C 60 modified TiO_2 nanocomposite photocatalysts, Bull. Korean Chem. Soc. 34 (2013) 3671–3676, https://doi.org/10.5012/bkcs.2013.34.12.3671.

[49] Z. Peining, A.S. Nair, Y. Shengyuan, P. Shengjie, N.K. Elumalai, S. Ramakrishna, Rice grain-shaped TiO_2–CNT composite—a functional material with a novel morphology for dye-sensitized solar cells, J. Photochem. Photobiol. A: Chem. 231 (2012) 9–18, https://doi.org/10.1016/J.JPHOTOCHEM.2012.01.002.

[50] S. Mu, Y. Long, S.-Z. Kang, J. Mu, Surface modification of TiO_2 nanoparticles with a C60 derivative and enhanced photocatalytic activity for the reduction of aqueous Cr (VI) ions, Catal. Commun. 11 (2010) 741–744, https://doi.org/10.1016/J.CATCOM.2010.02.006.

[51] W. Wang, P. Serp, P. Kalck, J.L. Faria, Photocatalytic degradation of phenol on MWNT and titania composite catalysts prepared by a modified sol–gel method, Appl. Catal. B Environ. 56 (2005) 305–312, https://doi.org/10.1016/J.APCATB.2004.09.018.

[52] M.S.A. Sher Shah, A.R. Park, K. Zhang, J.H. Park, P.J. Yoo, Green synthesis of biphasic TiO_2-reduced graphene oxide nanocomposites with highly enhanced

photocatalytic activity, ACS Appl. Mater. Interfaces 4 (2012) 3893–3901, https://doi.org/10.1021/am301287m.
[53] W. Fan, Q. Lai, Q. Zhang, Y. Wang, Nanocomposites of TiO_2 and reduced graphene oxide as efficient photocatalysts for hydrogen evolution, J. Phys. Chem. C 115 (2011) 10694–10701, https://doi.org/10.1021/jp2008804.
[54] M. Grätzel, A. Low Cost, High efficiency solar cell based on dye-sensitized colloidal TiO_2 films, Nature 353 (1991) 737–740.
[55] M.S. Dresselhaus, A. Jorio, A.G. Souza Filho, A.R. Saito, Defect characterization in graphene and carbon nanotubes using Raman spectroscopy, Philos. Trans. A Math. Phys. Eng. Sci. 368 (2010) 5355–5377, https://doi.org/10.1098/rsta.2010.0213.
[56] A. Jorio, E.H.M. Ferreira, M.V.O. Moutinho, F. Stavale, C.A. Achete, R.B. Capaz, Measuring disorder in graphene with the G and D bands, Phys. Status Solidi 247 (2010) 2980–2982, https://doi.org/10.1002/pssb.201000247.
[57] A.C. Ferrari, D.M. Basko, Raman spectroscopy as a versatile tool for studying the properties of graphene, Nat. Nanotechnol. 8 (2013) 235–246, https://doi.org/10.1038/nnano.2013.46.
[58] L.M. Malard, M.A. Pimenta, G. Dresselhaus, M.S. Dresselhaus, Raman spectroscopy in graphene, Phys. Rep. 473 (2009) 51–87, https://doi.org/10.1016/J.PHYSREP.2009.02.003.
[59] A.C. Ferrari, Raman spectroscopy of graphene and graphite: disorder, electron–phonon coupling, doping and nonadiabatic effects, Solid State Commun. 143 (2007) 47–57, https://doi.org/10.1016/J.SSC.2007.03.052.
[60] M.S. Dresselhaus, G. Dresselhaus, R. Saito, A. Jorio, Raman spectroscopy of carbon nanotubes, Phys. Rep. 409 (2005) 47–99, https://doi.org/10.1016/j.physrep.2004.10.006.
[61] P.T. Araujo, M. Terrones, M.S. Dresselhaus, Defects and impurities in graphene-like materials, Mater. Today 15 (2012) 98–109, https://doi.org/10.1016/S1369-7021(12)70045-7.
[62] L. Jin, B. AlOtaibi, D. Benetti, S. Li, H. Zhao, Z. Mi, A. Vomiero, F. Rosei, Near-infrared colloidal quantum dots for efficient and durable photoelectrochemical solar-driven hydrogen production, Adv. Sci. 3 (2016) 1500345, , https://doi.org/10.1002/advs.201500345.
[63] J.-W. Lee, S. Makuta, S. Sukarasep, J. Bo, T. Suzuki, Electron injection from a CdS quantum dot to a TiO_2 conduction band as an efficiency limiting process: comparison of QD depositions between SILAR and linker assisted attachment, J. Photopolym. Sci. Technol. 29 (2016) 357–362, https://doi.org/10.2494/photopolymer.29.357.
[64] W. Nan, Y. Niu, H. Qin, F. Cui, Y. Yang, R. Lai, W. Lin, X. Peng, Crystal structure control of zinc-blende CdSe/CdS core/shell nanocrystals: synthesis and structure-dependent optical properties, J. Am. Chem. Soc. 134 (2012) 19685–19693, https://doi.org/10.1021/ja306651x.
[65] G.S. Selopal, H. Zhao, X. Tong, D. Benetti, F. Navarro-Pardo, Y. Zhou, D. Barba, F. Vidal, Z.M. Wang, F. Rosei, Highly stable colloidal “Giant” quantum dots sensitized solar cells, Adv. Funct. Mater. 27 (2017) 1701468, , https://doi.org/10.1002/adfm.201701468.
[66] J. Bisquert, A. Zaban, P. Salvador, Analysis of the mechanisms of electron recombination in nanoporous TiO_2 dye-sensitized solar cells. Nonequilibrium steady-state statistics and interfacial electron transfer via surface states, J. Phys. Chem. B 106 (2002) 8774–8782, https://doi.org/10.1021/jp026058c.
[67] M. Adachi, M. Sakamoto, J. Jiu, Y. Ogata, S. Isoda, Determination of parameters of electron transport in dye-sensitized solar cells using electrochemical impedance spectroscopy, J. Phys. Chem. B 110 (2006) 13872–13880, https://doi.org/10.1021/jp061693u.
[68] W.H. Leng, Z. Zhang, J.Q. Zhang, C.N. Cao, Investigation of the kinetics of a TiO_2 photoelectrocatalytic reaction involving charge transfer and recombination through surface states by electrochemical impedance spectroscopy, J. Phys. Chem. B 109 (2005) 15008–15023, https://doi.org/10.1021/jp051821z.
[69] W. Wang, P. Serp, P. Kalck, J.L. Faria, Visible light photodegradation of phenol on MWNT-TiO_2 composite catalysts prepared by a modified sol-gel method, J. Mol. Catal. A Chem. 235 (2005) 194–199, https://doi.org/10.1016/j.molcata.2005.02.027.
[70] R. Asahi, T. Morikawa, T. Ohwaki, K. Aoki, Y. Taga, Visible-light photocatalysis in nitrogen-doped titanium oxides, Science 293 (2001) 269–271, https://doi.org/10.1126/science.1061051.
[71] S. Zhang, H. Niu, Y. Lan, C. Cheng, J. Xu, X. Wang, Synthesis of TiO_2 nanoparticles on plasma-treated carbon nanotubes and its application in photoanodes of dye-sensitized solar cells, J. Phys. Chem. C 115 (2011) 22025–22034, https://doi.org/10.1021/jp206267x.